

# Studies in large-eddy simulations of the NASA transonic Common Research Model

By K. Goc, R. Agrawal, S. T. Bose<sup>†</sup> AND P. Moin

## 1. Motivation and objectives

This brief describes the use of large eddy simulation (LES) in the context of external aerodynamic flows over the transonic NASA Common Research Model (CRM), which has been the focus of several Drag Prediction Workshops (DPWs) (Levy *et al.* 2003; Laffin *et al.* 2005; Vassberg *et al.* 2008, 2010; Levy *et al.* 2013; Tinoco *et al.* 2018). Sensitivities to laminar-to-turbulent transition, symmetry plane boundary condition, grid topology and subgrid-scale modeling approach are established and suggestions for best practices are made. Simpler problems such as a Blasius boundary-layer flow on a flat plate are studied in order to draw conclusions pertaining to transition behavior in a controlled environment. It is found that promoting the transition to turbulence via an array of cylindrical trip dots, using the full span of the aircraft, including the sting mounting system in the simulations and leveraging prismatic boundary-layer grids all tend to improve the quality of the LES solutions in this flow regime. For the first time, novel non-Boussinesq subgrid-scale models and sensor-based wall models are applied to a complex external flow over an aircraft with promising results on coarse grids numbering about 100 million control volumes (Mcv). As has been observed in canonical smooth-body separation problems, nonmonotonic grid convergence in wall-modeled LES continues to be an issue for problems of engineering interest, with finer grid solutions (up to 750 Mcv) performing worse than their coarse-grid counterparts. The details of the boundary-layer profiles both at the leading edge of the wing and within the shock-induced separation bubble are studied, with thicknesses and integral measures reported. The brief is organized as follows. In Section 2, details on the flow solver, validation case, and simulation cases are given. In Section 3.1 we describe validation efforts at appropriate modeling of experimental trip dots in LES calculations of transonic flows. In Section 3.2, we describe the extension of these heuristics to a full transonic CRM aircraft configuration. Next, the sensitivities to the symmetry plane, grid topology, and subgrid-scale/wall model are established in Sections 4, 5, and 6 respectively. Assessments of the boundary-layer characteristics of the flow over this realistic aircraft configuration are made in Section 7. Finally, conclusions are drawn in Section 8.

## 2. Background

### 2.1. Flow solver

LES techniques are used to simulate the transonic flows presented herein. These methods directly resolve the large scales of turbulence and rely on closure models to account for the impact of turbulence in the subgrid regime. The solver employed is charLES (Ham

<sup>†</sup> Cascade Technologies, Inc. and Institute of Computational and Mathematical Engineering, Stanford University

*et al.* 2006), a second-order, low-dissipation finite-volume solver. We solve the governing equations for a low-pass filtered, compressible Navier–Stokes system for mass, momentum and total energy. The numerical scheme has been shown to be suitable for coarsely resolved large-eddy simulations of turbulent flows that are especially sensitive to numerical dissipation. The discretization is suitable for arbitrary unstructured, polyhedral meshes, and the solutions contained herein are computed from unstructured grids based on Voronoi diagrams. The use of Voronoi diagram–based meshes allows for the rapid generation of high-quality grids with some guaranteed properties (for instance, the vector between two adjacent Voronoi sites is parallel to the normal of the face that they share). Time advancement is performed using a three-stage explicit Runge-Kutta scheme (Gottlieb *et al.* 2001), and the spatial discretization is formally second-order accurate. Additional details of the numerical discretization and grid generation can be found in Fu *et al.* (2021), Lozano-Duran *et al.* (2020) and Bres *et al.* (2018). In this report, subgrid closures are modeled using the Dynamic Smagorinsky approach of Germano *et al.* (1991) unless otherwise noted. Also unless otherwise noted, near-wall regions are modeled using an equilibrium wall model that assumes that the pressure gradient is balanced by the advective term, leading to a constant stress layer (Bose & Park 2018) within the modeled region. A stress is applied at the wall based on an assumed log-law in the boundary-layer profile.

## 2.2. Validation case: NASA transonic CRM

The reference conditions for the calculations presented herein are  $Re = 5.0e6$ ,  $M = 0.85$  and  $\alpha = 2.50^\circ - 4.0^\circ$  spaced at  $0.25^\circ$  increments. The Reynolds number is typical of wind tunnel conditions for transonic aircraft experiments. The reference data used is from the investigations of Rivers & Dittberner (2010) at the NASA Langley National Transonic Facility (NTF), an image of which is shown in Figure 1. In all calculations conducted in this brief, the aeroelastic deflection reported in Tinoco *et al.* (2018) is used for the baseline geometries, resulting in new meshes and wing deformations for each angle of attack simulated, with up to  $6.5''$  of wingtip deflection (at full scale) having been observed between the lowest angle of attack, the  $\alpha = 2.50^\circ$  case, and the highest angle of attack, the  $\alpha = 4.00^\circ$  case. At full scale, the aircraft mean aerodynamic chord (MAC) has a length of  $275.8''$ , while the wingspan takes on a value of  $2313.5''$ . The aspect ratio of the wing is 9 and the leading edge is swept at an angle of  $35^\circ$  relative to the horizontal. The calculations described herein are run in a free air setting, because insufficient characterization of the NTF wind tunnel geometry is currently available in the open domain; however, the sting mounting system visible at the tail of the aircraft in Figure 1 is included in several of the simulations and improved shock locations have been observed upon inclusion of this feature, though it is not discussed in any more detail in this brief. Although this case has been a focus in the external aerodynamics community for many years, emerging paradigms such as LES have been used very sparsely to date on this configuration. The work of Lehmkuhl *et al.* (2016) was among the first of such efforts, which showed promising initial results on coarse grids at one angle of attack. More recent work by Ghate *et al.* (2021) studied the influence of the Vreman (2004) subgrid-scale model coefficient choice on the shock location and found limited sensitivity to this choice. It was clear from these studies that further investigation into the treatment of turbulent transition, grid resolution and subgrid-scale modeling approach are needed to build confidence in the predictive capabilities of LES in this flow regime. The aim of this brief is to address these issues.

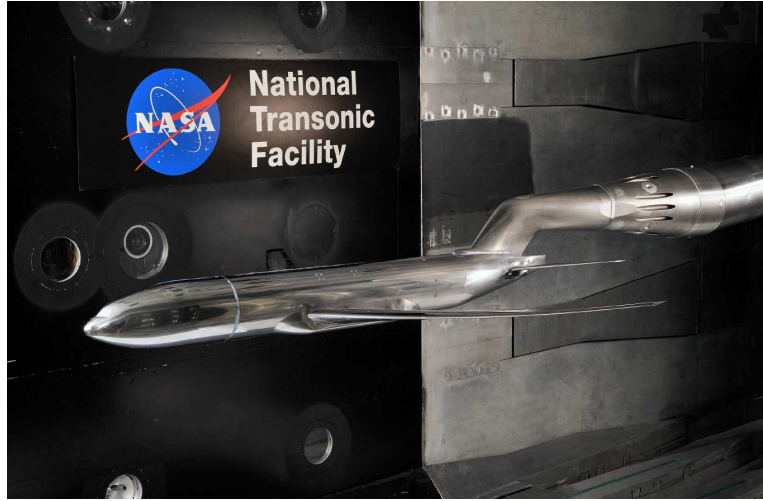


FIGURE 1. Image of the experimental apparatus from the NTF wind tunnel runs used as reference data in this brief. Reproduced from Rivers & Dittberner (2010).

TABLE 1. Details of the geometric features represented on each mesh and the associated grid counts. The meshes are given a label A–E.

	50 Mcv HCP Mesh (A)	100 Mcv HCP Mesh (B)	750 Mcv HCP Mesh 1 (C)	750 Mcv HCP Mesh 2 (D)	270 Mcv Strand Mesh (E)
Full/Half Span	Half	Full	Full	Full	Half
Trip Dots	Excluded	Excluded	Included	Excluded	Excluded
Sting Mount	Included	Included	Included	Included	Excluded
Aeroelastic Deflection	Included	Included	Included	Included	Included

### 2.3. Description of grids used

This subsection is meant to provide clarity on the meshes used in the subsequent sections of the brief, explicating the geometric features represented on each mesh. Table 1 describes the details of the geometric features of the NASA CRM represented in each of the five meshes and the associated grid counts. The meshes used in each section are as follows: Section 3.2 uses meshes C and D, Section 4 uses meshes A and B, Section 5 uses meshes C and E, Section 6 uses meshes B and C, while Section 7 uses mesh E.

## 3. Importance of turbulent transition

### 3.1. Trip dot validation on a flat plate

It is fundamentally important to understand the role of trip dots in promoting transition in canonical problems such as the flow over a flat-plate boundary-layer. This analysis will anchor our investigations of the grid requirements for resolving trip dots in more complex

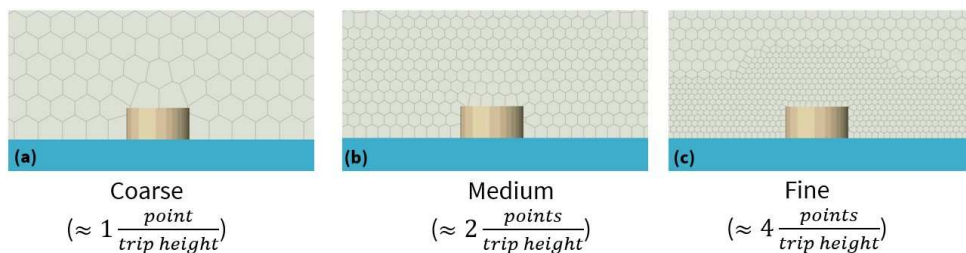


FIGURE 2. Spanwise slices of the three grids considered for the single trip dot calculations, ranging from a (a) coarse grid with just 1 point per trip dot height to (b) a medium grid with 2 points per trip height and (c) a fine grid with 4 points per trip dot height.

flows such as full-scale aircraft. For this purpose, based on the experiment of Ichimiya *et al.* (1993), a single trip dot is placed in a laminar boundary-layer, and the wake spreading angle of the disturbed flow and the impact of the trip dot on skin friction ( $\tau_w$ ) are measured. Ichimiya *et al.* (1993) reported that the wake-spreading angle (measured as the angle between the symmetry plane and the edge of the wake) behind a single trip dot varied from  $4.8^\circ - 6.0^\circ$  (depending on the height above the wall where the wake was measured) at a Reynolds number,  $Re_k$ , based on the trip dot height of 1000.

To replicate the laminar experimental inflow conditions, a Blasius boundary-layer solution is fed as the inflow to the LES simulation. The inlet boundary-layer thickness is adjusted such that the extrapolated boundary-layer thickness at the location of the trip exactly matches the experimental boundary-layer thickness, which was the same as the trip height (2 mm). Three grid resolutions, as shown in Figure 2, were examined in this work. Note that the grids are isotropically refined by a factor of two to up to 4 points per trip dot height. The primary reason for not evaluating further grid sensitivities is based on the maximum achievable resolution attainable on the full aircraft configuration. For example, even a fine grid with 4 points per trip dot height would approximately scale to 2 billion control volumes on the full aircraft simulation. The wake-spreading angles for the three considered grids are reported in Figure 3. It is clear that the coarsest grid fails to capture any meaningful impact associated with the trip dot, as patterned bands of transition appear at regularly spaced intervals that approximately match the grid spacing, meaning that the transition is almost entirely grid-induced in this case. On the medium mesh with 2 points per trip dot height, some impact of the trip dot is visible, with transition occurring earlier than in the untripped regions of the flow. Further, the interaction of the grid with the periodic boundary face leads to disturbances injected from the spanwise boundaries that contaminate the rest of the flowfield. Finally, with 4 points per trip dot height, a clean wake with a spreading angle of  $4.5^\circ$  is obtained, which is in reasonable agreement with the experimental results (Ichimiya *et al.* 1993).

A further quantitative assessment of the influence of the trip dot on the flowfield was made by evaluating the streamwise skin friction evolution through the centerline of the domain, shown in Figure 4. Several comparisons are encapsulated in this plot, including the impact of the trip dot on a plug inflow and the impact on an inflow having a Blasius boundary-layer. An important conclusion is that regardless of the inflow chosen, the trip dot successfully promotes an elevated level of skin friction in the wake of the trip dot. This elevated level persists far downstream of the trip dot. This study of the sensitivity to the influence of the inflow conditions is motivated from evidence that for a flow over an aircraft wing, the boundary-layer profile upstream of the trip dots is not necessarily

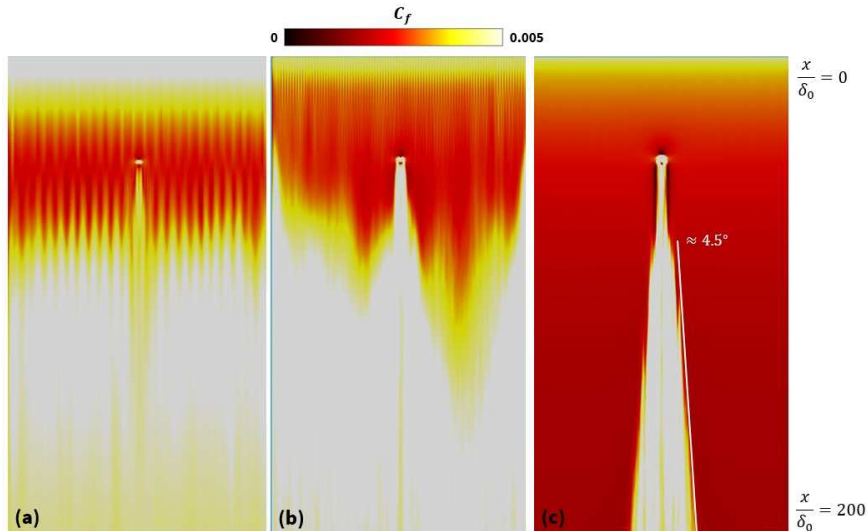


FIGURE 3. Surface contours of the average skin friction for the single trip dot flat-plate calculations ranging from (a) a coarse grid with just 1 point per trip dot height, (b) a medium grid with 2 points per trip dot height and (c) a fine grid with 4 points per trip dot height. The flow is from top to bottom and extends approximately 200 inlet boundary-layer thicknesses in this visualization.

well-known. In this sense, the plug inflow serves as an extreme case of an underresolved thin boundary-layer ahead of the trip dot. It is promising that the trip dots can promote a transition-like event even for this inflow. In addition, note that for the untripped case, the flow remains laminar throughout the simulation, which confirms that numerical noise or perturbations in the grid are not leading to transition in this setting.

Finally, we note that the untripped cases approach the same asymptotic skin friction value far downstream, while the tripped cases retain some memory of the inflow, with the plug inflow case retaining a larger skin friction value downstream of the trip dot than the case that had the Blasius boundary-layer at the inlet. This difference in the turbulent state between the tripped cases with differing inlet conditions was at most 10% and was not explored further in this study, as this level of control over the oncoming state of the boundary-layer ahead of the trip dot is not practical in a full aircraft configuration. This sensitivity does, however, provide some indication of the amount of error that could propagate into the wake of the trip dots due to underresolved leading-edge boundary-layers. Based on these findings, we selected 4 grid points as an entry point into trip dot resolving simulations in external aerodynamics at  $Re_k$  of order 1000, which is typical in wind tunnel experiments of aircraft (Rivers & Dittberner 2010; Evans *et al.* 2020).

### 3.2. Impact of trip dots on the NASA transonic CRM

With the single trip dot validation case complete, the influence of the full array of trip dots was explored on the transonic CRM configuration. In transonic external aerodynamics problems, experiments conducted at wind tunnel Reynolds numbers require physical tripping either via trip dots, active blowing/suction or surface roughness to achieve comparable boundary-layer characteristics to realistic flight Reynolds number conditions (Rivers & Dittberner 2010). The wind tunnel data used as a reference in this study were collected at the NASA Langley National Transonic Facility (NTF) and used cylindrical

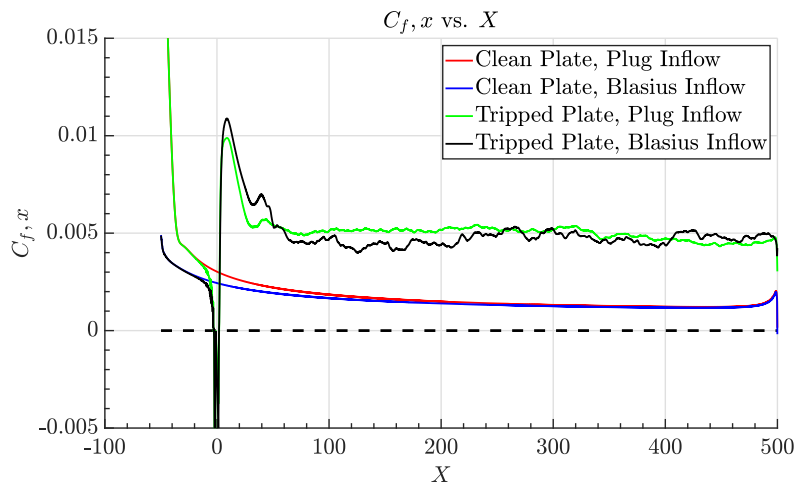


FIGURE 4. Centerline slice of time-averaged streamwise component of skin friction plotted against the streamwise direction normalized by the inlet boundary-layer thickness, ( $X = \frac{x}{\delta_0}$ ) on the fine grid, which has 4 points per trip dot height. The location  $X = 0$  is at the point of the trip dot.

trip dots to promote transition in the flow over the CRM. These trip dots were placed at 10% of the local chord on the suction side of the wing along the entirety of the span as well as near the fuselage nose. The trip dots were made of a vinyl adhesive material and measured just  $0.003'' - 0.0035''$  at model scale (Rivers *et al.* 2015) (alternatively, the trip dot heights could be viewed as a percentage of the mean aerodynamic chord length of  $7.447''$ , in which case they would be between  $\approx 0.04\% - 0.045\%$  of a chord length in their height). They measured  $0.05''$  in diameter and were spaced at a distance of  $0.1''$  apart, resulting in a total of  $\approx 315$  total trip dots along the span of the wing, which was  $63.47''$  in length at model scale. These trip dots were added to the baseline CRM geometry using a CAD tool, and they match the experimental dimensions, spacing and location exactly, as provided in Rivers & Dittberner (2010). Figure 5 shows the qualitative impact of this trip dot array. We can see from this image that the trip dots are effective at promoting an earlier and more consistent transition front. In these cases, the wake spreading observed in the single trip dot case is not reproduced, potentially owing to the aggregate effect of the trip dot array suppressing this mechanism. The location at which the projected first cell velocity abruptly changes from light to dark is the shock location. At this point, the strong adverse pressure gradient of the shock strongly decelerates the flow and the turbulent structures grow rapidly in size.

A quantitative assessment of the influence of the trip dots is shown in Figure 6 by means of the surface pressure coefficient. Reference experimental data from the NTF (Rivers *et al.* 2015). The grids for the trip dot-resolving and clean wing cases are identical except in the immediate vicinity of the trip dots and are both number about 750 Mcv (Meshes C & D). Due to computational cost considerations, a full 4 points per trip dot-height resolution was not possible, as the flat-plate calculations indicated was necessary. Instead, approximately 3 points were used to resolve the trip dot height. Despite this marginal resolution level, the earlier transition associated with the inclusion of trip dots on the CRM wing led to improved shock locations relative to the experimental data on the suction side of the wing. The perturbation in the  $C_p$  plot around  $10\% x/c$  reflects

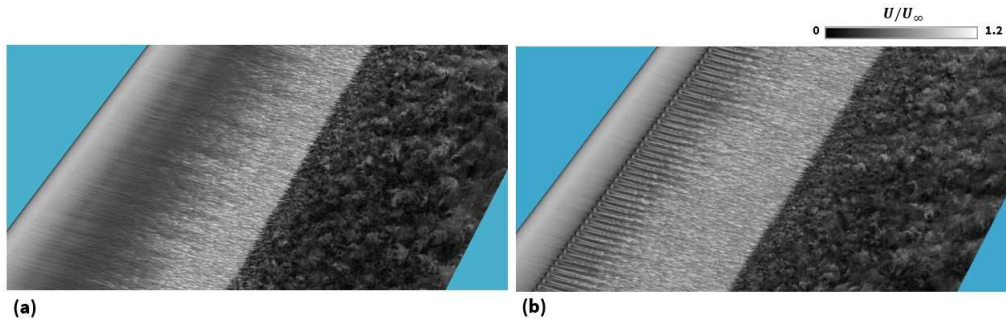


FIGURE 5. Instantaneous velocity magnitude projection on the suction side of the Transonic CRM wing showing (a) an untripped and (b) a tripped case where trip dots have been placed along the entire span of the wing at a constant spanline of 10%. Flow is from left to right.

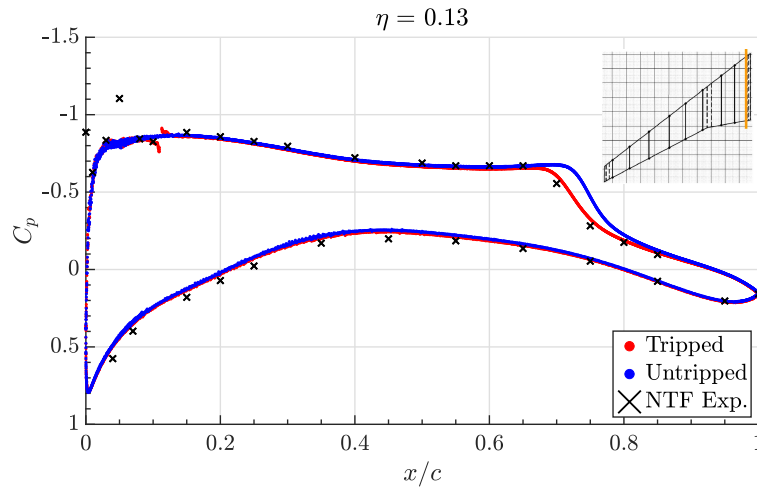


FIGURE 6. Average pressure coefficient slice through an inboard wing station at  $\alpha = 4^\circ$  showing the impact of the wing trip dots. The earlier shock location observed in the tripped case is consistent with the experimental measurements. The vertical orange line in the inset graphic shows the location of the pressure cut along the span of the wing.

the location at which the trip dots are installed in the simulations. Overall, these numerical experiments highlight the importance of laminar-to-turbulent transition in transonic external aerodynamic flows over aircraft, suggesting that careful representation and grid resolution around these protuberances are necessary to accurately predict engineering quantities of interest such as pressure coefficients in transonic aircraft flows.

#### 4. Impact of symmetry plane boundary condition

It is the standard practice of the external aerodynamics community to perform aircraft simulations on a half-span domain using a symmetry plane boundary condition on the center plane to save on computational cost. This has been the baseline approach for the duration of the High-Lift (Rumsey *et al.* 2011; Rumsey & Slotnick 2015; Rumsey *et al.* 2019, 2022) and Drag Prediction (Levy *et al.* 2003; Laffin *et al.* 2005; Vassberg *et al.* 2008, 2010; Levy *et al.* 2013; Tinoco *et al.* 2018) workshop series. These practices, however,

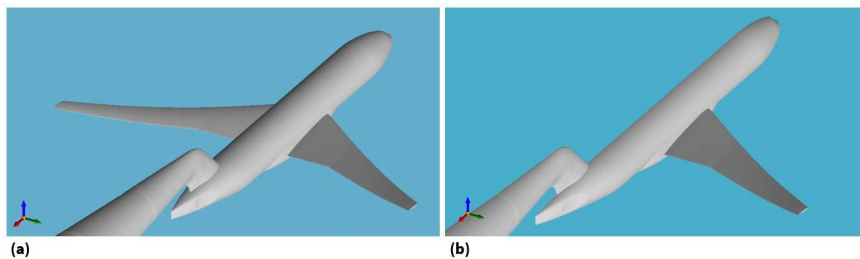


FIGURE 7. Geometry of the Transonic CRM including (a) the full span and including (b) a symmetry plane. This configuration will be used to evaluate the sensitivity of the LES calculations to the center plane boundary condition.

are established for steady-state Reynolds-Averaged Navier Stokes (RANS) simulations in which instantaneous turbulent fluctuations are not explicitly resolved. In LES, a study of the appropriate symmetry plane treatment needs to be conducted, as turbulent fluctuations on the fuselage that traverse the center plane violate instantaneous symmetry even if the time-averaged flow is symmetrical in the span. For this reason, an exploration on relatively coarse grids (Meshes A & B) was performed to establish sensitivities to the symmetry plane boundary condition. Figure 7 shows the differences between these where the full-span case is simply the half-span case that includes the mirrored part of the domain.

A sensitivity of the time-averaged flowfield to the treatment of the symmetry plane is found to be present for these calculations, with the full-span simulations showing improved characterization of the shock structure relative to the half-span cases, as shown in Figure 8. Surprisingly, the largest differences between the sectional pressure measurements are concentrated on the outboard part of the wing ( $\eta \approx 0.5$  and beyond). One might expect that the strongest differences between the cases would be observed near the symmetry plane; however, we find the opposite: that large changes in the shock structure are concentrated near the wingtip, potentially owing to the 2D-type versus 3D-type shock-relieving effect often studied in supersonic flows over cylinders and spheres (Bryson & Gross 1961).

Significant instantaneous asymmetries in the rolling moment (computed about the  $x$ -axis passing through the fuselage nose) do arise in this flow despite the time-averaged rolling moment being approximately zero. Figure 9 shows a plot of rolling and pitching moments over the course of a simulation horizon of 100 flow passes based on the mean aerodynamic chord. The instantaneous oscillations in the rolling moment are larger than those in the pitching moment. We find on the basis of these simulations that while the time-averaged value of the rolling moment is nearly zero, it is inadequate to perform the calculations half span and use a symmetry plane boundary condition due to the presence of significant instantaneous asymmetries in the turbulent flowfield.

Finally, the integrated forces and moments are compared in Figure 10. It is clear from this plot that for a given grid, the full-span configuration is in better agreement with experiment than the half-span case. This result is found on a relatively coarse grid that is sized to fit 512 grid points across the mean aerodynamic chord. Further studies related to grid refinement and grid topology sensitivities will be established later in the report. However, we conclude on the basis of this experiment that symmetry plane effects are important for LES simulations of transonic aircraft flows and recommend the use of full-span domains.

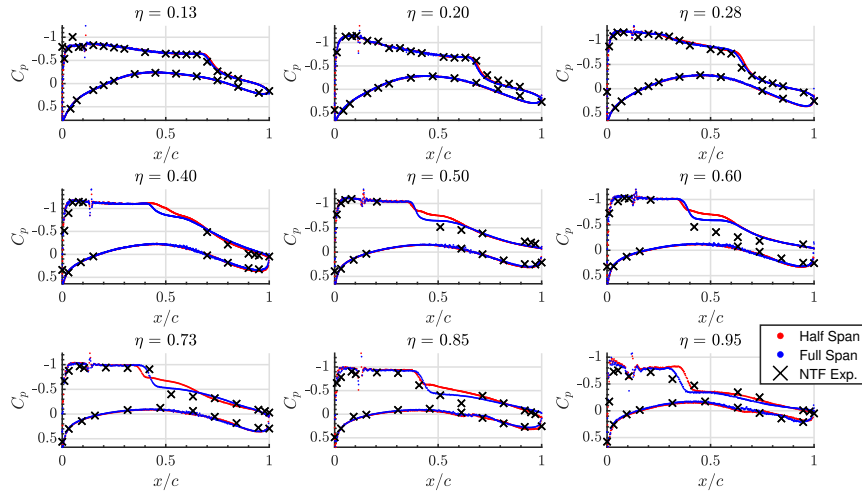


FIGURE 8. Spanwise pressure measurements for the half-span versus full-span Transonic CRM calculations. The largest differences between the half-span and full-span calculations are observed starting mid-span and moving outboard.

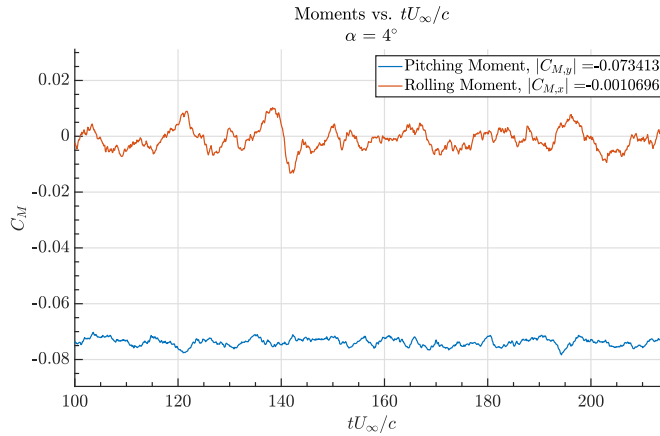


FIGURE 9. Rolling and pitching moments on the Transonic CRM for the full-span case. Instantaneous asymmetries in the rolling moment are observed despite the time-averaged value being near zero.

### 5. Sensitivity to grid topology

The shock location in transonic flows is sensitive to the details of the boundary-layer because the shock location is set by the inviscid acceleration (dictated by the effective body shape in which viscous effects are important). For this reason, a grid that used prismatic boundary-layer elements in which additional refinement in the wall-normal direction was explored (see Figure 11 for a schematic). Prismatic-type boundary-layer elements (hereinafter referred to as stranded grids) have the advantage over isotropic hexagonally close-packed (HCP) meshes in viscous regions because it is possible with this grid topology to stretch the mesh in the wall-normal direction in order to resolve the

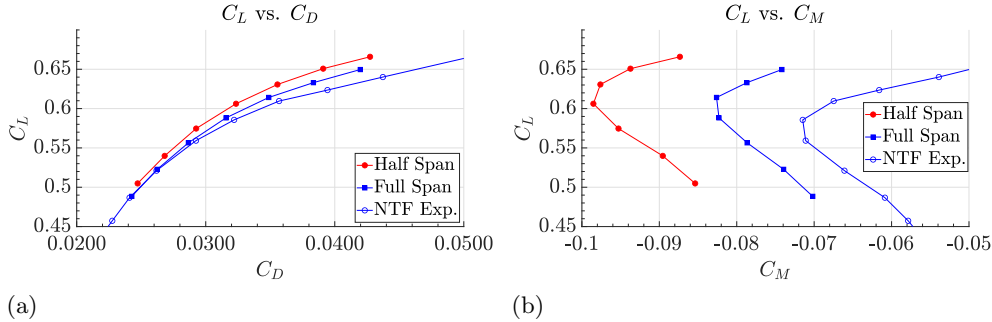


FIGURE 10. Non-dimensional (a) drag polar, and (b) lift versus pitching moment coefficient plots for the half-span and full-span LES cases compared against experimental data from the NTF tunnel (Rivers *et al.* 2015). The simulations are run on a  $\approx 50$ -Mcv mesh in the half-span case (Mesh A) that is mirrored about the symmetry plane when the case is run in full-span mode (Mesh B). In each metric, the full-span simulations outperform the half-span ones.

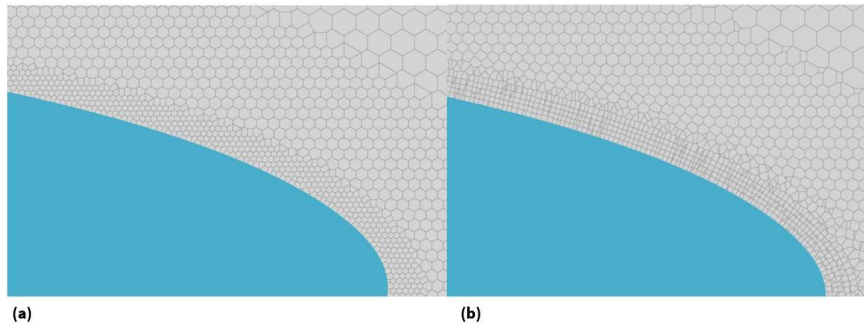


FIGURE 11. Slice through the leading edge of the CRM wing showing (a) the default HCP grid topology and (b) a modified stranded mesh in the wall-adjacent region.

vertical length scale of the wall-bounded turbulence, which shrinks at a faster rate than the streamwise or transverse length scales in the boundary-layer as the wall is approached (Marusic & Monty 2019).

Figure 11 shows a comparison between an isotropic HCP and an isotropic strand-mesh. Further explorations of appropriate anisotropy ratios for stranded mesh calculations were conducted, and it was found that superior performance of the solution on the stranded mesh was achieved for an anisotropy ratio of 4:1 and a maximum wall-normal stretching ratio of 1.15. Also concluded from this study was the importance of the wall-model LES exchange location on stranded meshes, and all stranded cases presented in this report use a second cell centroid exchange height. This same sensitivity was not observed on HCP meshes, and all HCP calculations therefore used the first cell centroid as the exchange height. Figure 12 shows the result of this sensitivity exploration to grid topology. The HCP and strand cases were not chosen to be analogous in terms of point count/cell size; instead, they should be viewed as the best achievable result with each topology at the bleeding edge of computing affordability on modern GPU computing resources. The stranded-mesh (Mesh E) result reported in Figure 12 has  $2\times$  finer wall-normal resolution, while being  $2\times$  coarser in the stream/spanwise directions than the reference HCP solution (Mesh C). Additionally, because of the difficulty associated with creating a high-quality

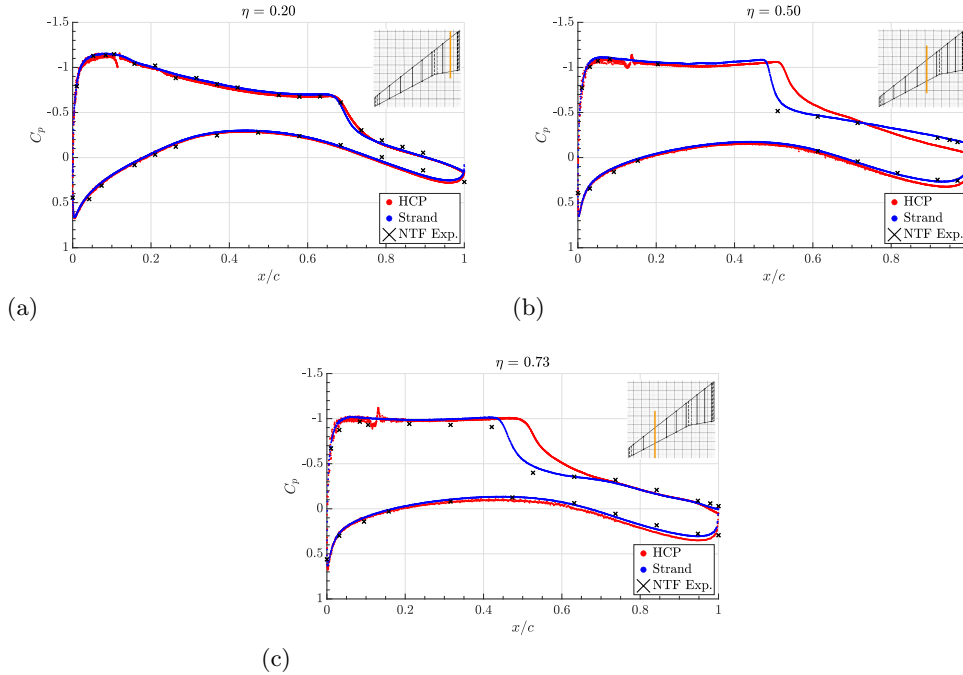


FIGURE 12. Average static pressure measurements for the Transonic CRM at an angle of attack of  $\alpha = 4.0^\circ$  at three different stations along the span of the wing, ranging from (a) inboard to (b) mid-span to (c) outboard. The comparison includes results computed on a fine mesh of isotropic HCP grid elements ( $\approx 750$  Mcv, Mesh C) and a strand mesh solution that is  $2\times$  finer than the HCP mesh in the wall-normal direction and  $2\times$  coarser in the stream/spanwise directions ( $\approx 270$  Mcv, Mesh E).

prismatic mesh around the leading-edge trip dots, these have been removed from the stranded calculations.

Further comparison was made to the surface flow patterns predicted by each mesh topology, shown in Figure 13. Experimental reference data for the surface flow was not available, so OVERFLOW RANS data are shown as a benchmark. The RANS data represent a best practice result from the Sixth Drag Prediction Workshop (DPW6) contribution of the Boeing Southern California group using the OVERFLOW solver. The Spalart-Allmaras turbulence model with Quadratic Constitutive Relation (SA-QCR) was used for the RANS simulations, a modeling practice known to perform well in this flow, particularly in the wing juncture region (Tinoco *et al.* 2018). The RANS calculations were run in fully turbulent mode with no explicit representation of the trip dots. The shock in this case is strong enough to induce a pocket of separation in the mid-span region, visible in the surface streamline patterns by the regions in which the streamlines become parallel to the trailing-edge sweep. The extent of the separation region from the HCP solution is smaller than the RANS solution (as was observed in the sectional pressure measurements that showed that the shock lies too far aft). In the stranded solution, the extent of the separation is approximately in agreement with the RANS solution, while the strength of the separation is more intense (lower values of skin friction magnitude in the bubble).

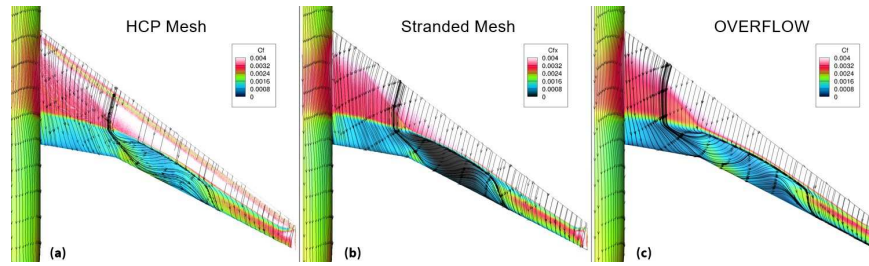


FIGURE 13. Average surface skin friction magnitude and surface streamlines from three simulations, including LES simulations with best-achievable solutions on (a) HCP meshes, (b) stranded Meshes and from (c) RANS simulations using the OVERFLOW solver.

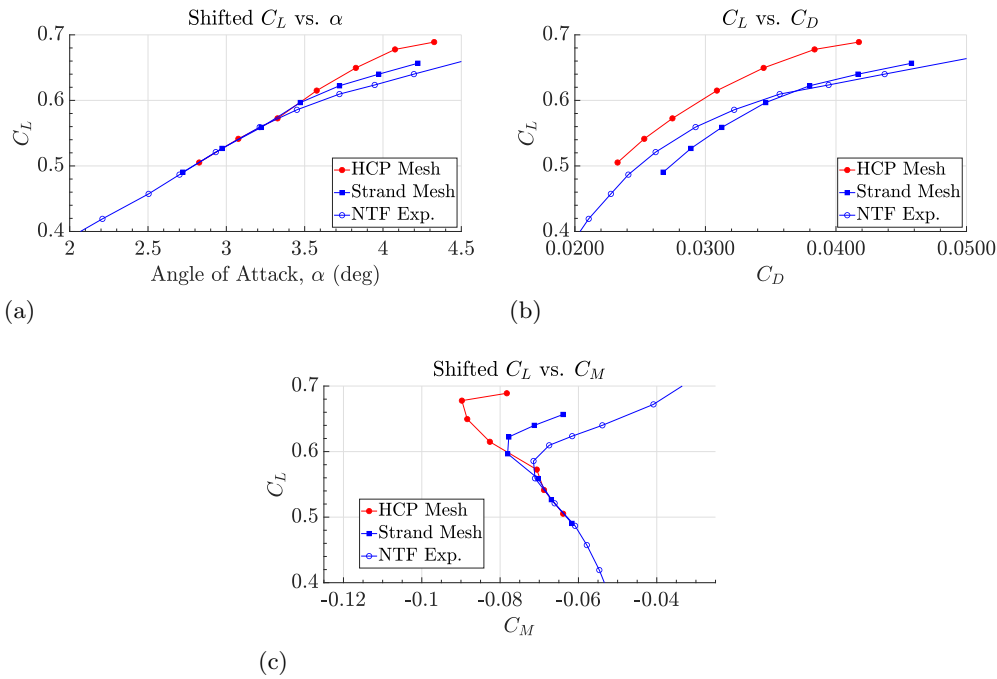


FIGURE 14. Average forces/moments from the LES simulations of the Transonic CRM, including (a) the shifted lift, (b) drag polar and (c) shifted pitching moment. The shifting of the lift and pitching moment plot is performed as suggested in Tinoco (2020).

Finally, the integrated forces/moments are compared against reference data in Figure 14. On the basis of these results, it is clear that stranded meshing offers advantages over HCP grids in transonic flows, particularly at higher angles of attack at which significant shock-induced separation is observed. However, the results from the best-practice strand mesh do still exhibit some degree of delay in the pitch break (where the  $C_M$  curve abruptly becomes less negative) in Figure 14(c) associated with a delay in the onset of shock-induced separation. Still, significant benefit is achieved from the use of stranded meshes in the prediction of lift, drag and pitching moment for this flow.

## 6. Novel modeling approaches

Novel subgrid-scale (SGS) and wall-modeling approaches for LES such as those discussed in Agrawal *et al.* (2022b) and Elnahas *et al.* (2022) have recently been developed and deployed on the transonic CRM to assess their applicability beyond canonical flows (including turbulent channel flows, flow over the Boeing speed bump and Sandia transonic hump). A key issue arising in wall-modeled LES calculations of external aerodynamic flows is the problem of nonmonotonic convergence of the quantities of interest. Most notably, on the Boeing Gaussian Bump flow, this has been a persistent issue with standard modeling approaches (Whitmore *et al.* 2021). Non-Boussinesq SGS models such as the Dynamic Tensor Coefficient Smagorinsky Model (DTCSM) developed by Agrawal *et al.* (2022b) have been shown to rectify this issue. Figure 15, however, shows a mixed result on this more complex flow. The prediction on a given grid is improved by the DTCSM SGS + Sensor Wall Model, when compared to its Dynamic Smagorinsky + Equilibrium Wall Model (EQWM) counterpart. However, the deficiency of the coarse-grid result being more accurate than the fine-grid result is still observed. The inclusion of a recently developed sensor-aided equilibrium wall model (Agrawal *et al.* 2022a) is aimed at identifying regions of strong adverse pressure gradients. In these regions, the model includes the subgrid-stress in addition to the equilibrium wall-modeled stress when prescribing the total wall stress. This method is developed as a proxy to account for the non-zero resolved stresses on the wall and has been successfully applied to the case of the Boeing speed bump. It is clear that while at this juncture novel modeling approaches such as those developed in Agrawal *et al.* (2022b) provide tangible benefits over standard modeling choices, the issue of nonmonotonic grid convergence is not fully rectified by these models on full-scale aircraft. Further study is needed to identify the reason behind this deficiency but may include the presence of compressibility effects, aircraft three dimensionality effects (finite span wing, spanwise pressure gradient) or Reynolds number differences.

The pressure measurements at the 4-degree condition are shown in Figure 16 from the coarse-grid and fine-grid DTCSM + Sensor WM cases (which are considered the best-practice modeling approach based on experience in canonical flow validations) and show that in general, the prediction of the lift and moment achieved on the coarse grid is approximately for the right reasons because the shock location is in good agreement with available experimental data on the coarse grid, while on the finer mesh, the shock moves aft, which is consistent with the collapse of the shock-induced separation bubble and leads to higher lift levels and more nose-down pitching moment tendencies.

## 7. Boundary-layer details

Although the engineering quantities of interest for the flow over an aircraft are integrated forces and moments, it is important to quantify the effect of the Reynolds numbers and pressure gradients in the development of the boundary-layer over the complex flow for informing modeling efforts. In this work, multiple wall-normal velocity profiles are collected and reported from one of the more accurate and refined calculations at the 4-degree angle of attack. These profiles are sampled at the leading edge of an inboard wing station (in order to understand the nature of the flow ahead of the shock and away from the separation bubble and wingtip effects) and within the separation bubble at mid-span. The wall-parallel velocity profiles ( $U_{||}$ ) are shown in Figure 17. The generalized, compressibility effects-inclusive, method developed in Griffin *et al.* (2021) is used

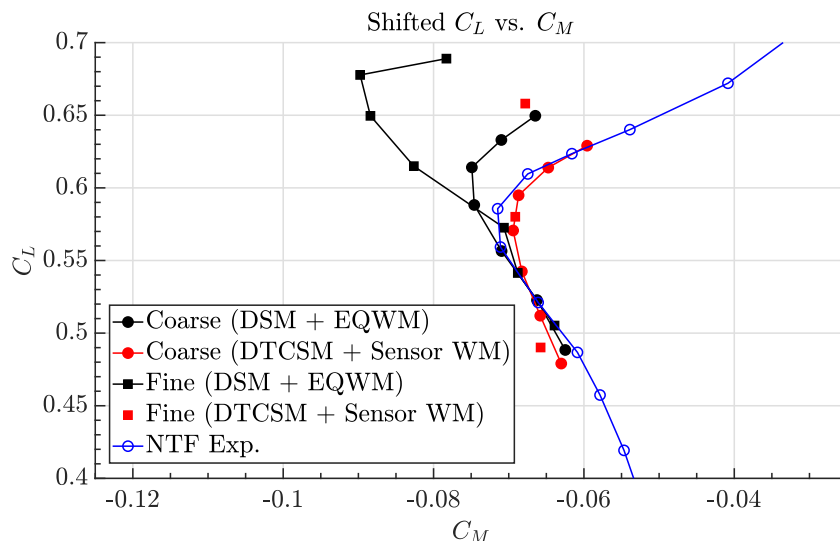


FIGURE 15. Average lift versus moment plot from the LES simulations of the Transonic CRM with results from novel SGS and Wall Models included in the plot. The shifting of the pitching moment plot is performed as suggested in Tinoco (2020).

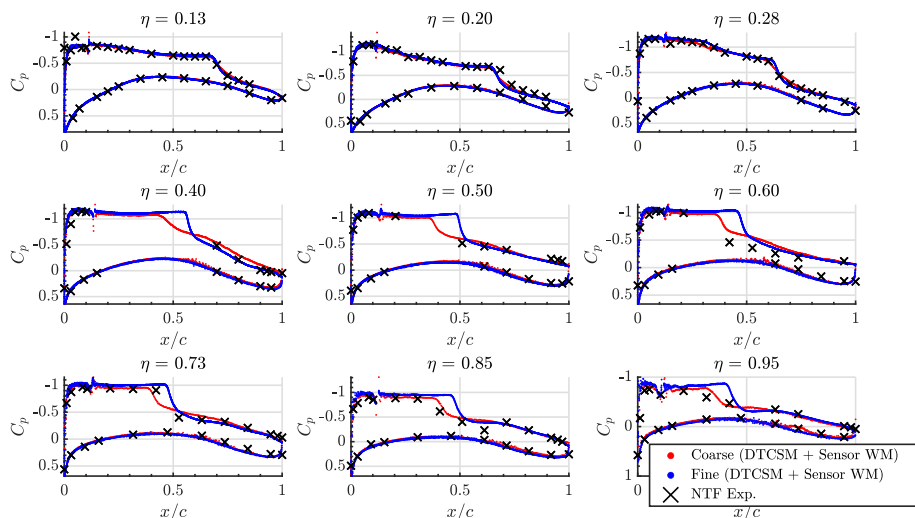


FIGURE 16. Sectional pressure measurements from the Sensor Wall Model + Dynamic Tensor Coefficient Smagorinsky Model calculations for the Transonic CRM at angle of attack of 4 degrees.

to evaluate the boundary-layer edge ( $\delta_{99}$ ). The point of maximum stagnation enthalpy ( $h_{0,ref}$ ) is used to establish the far-field conditions used in the method for computing the boundary-layer edge.

Table 2 shows the quantitative boundary-layer measures associated with Figure 17. Note that these numbers apply to full-scale aircraft at wind tunnel-type Reynolds num-

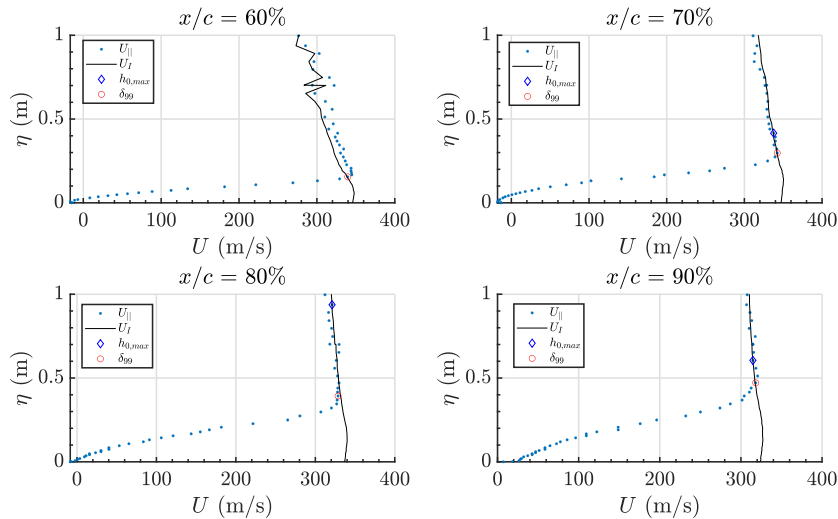


FIGURE 17. Wall-parallel velocity profiles at mid-span (50% of the semi-span) within the separation bubble. The boundary-layer edge is determined using the compressible method of Griffin *et al.* (2021) for flows in non-equilibrium.

bers (typically an order of magnitude smaller than the true flight Reynolds number). Although the experiment is at model scale, the simulations are run at full scale, which explains why the measures of boundary-layer parameters apply to a somewhat synthetic case of a full aircraft at wind tunnel Reynolds number. Still, the details of the boundary-layer characteristics will be informative from the perspective of understanding the character of the boundary-layer and for the selection of pertinent canonical cases for future reduced-order modeling efforts. It is apparent that the flow over an aircraft wing experiences a wide range of Reynolds numbers based on momentum thickness ( $Re_\theta$ ) and shape factors ( $H$ ), and suitable canonical cases must be chosen that are representative of these nondimensional measures. A different case must likely be chosen to represent the thin leading-edge flow, and a different case would be suitable for the thick separated flow near the trailing edge. Finally, even for the finest grids considered in this work, the thin leading-edge boundary-layers are marginally resolved with at most 5 grid points within the boundary-layer. This points to another important necessity of future LES modeling efforts: the need to predict quantities of interest with  $\mathcal{O}(5)$  points within the leading-edge boundary-layer.

## 8. Conclusions

In this article, we have described simulations of the transonic version of the NASA CRM, a benchmark flow for drag prediction and CFD validation in the compressible flow regime, representing a commercial aircraft in cruise configuration. These calculations are among the first forays into use of LES for this kind of flow, and initial heuristics were developed around best practices, including the use of an array of small cylindrical trip dots lining the leading edge of the wing at a constant spanline of 10% (which replicates the way that turbulent transition was achieved in the experiment), simulation of the fullspan configuration (which again matches the experimental setup), inclusion of the

TABLE 2. Boundary-layer characteristics for the Transonic CRM flow both near the leading edge (spanwise location 0.2) and within the separation bubble (spanwise location 0.5). A wide range of Reynolds numbers and shape factors are observed as the boundary-layer thickens and experiences shock-induced separation.

Spanwise Location	Chordwise Location (%)	$\delta_{99}$ (cm)	Shape Factor (H)	$Re_\theta$	$\frac{\delta}{\Delta}$
0.2	1	0.76	1.86	472	2
0.2	5	1.24	2.50	657	3
0.2	10	1.25	2.44	729	4
0.2	20	2.62	2.34	1,505	5
0.5	60	15.5	6.33	10,558	20
0.5	70	29.7	6.67	18,006	28
0.5	80	39.3	4.88	28,648	29
0.5	90	47.1	3.80	41,382	30

sting mounting apparatus at the tail of the aircraft and the use of prismatic boundary-layer grids of maximum anisotropy ratio of 4:1 in the wall-normal direction relative to the streamwise and spanwise directions. Also explored were the combination of a novel non-Boussinesq DTCSM subgrid-scale model and a sensor-based wall model that identifies regions of flow separation and aids the equilibrium wall model in providing a more reasonable account of the wall shear stress in those regions. The integrated effect of these models resulted in an improved characterization of the pitching moment break, particularly on coarse grids. The solutions were plagued by the problem of nonmonotonic grid convergence observed in canonical smooth-body separation flows, though the novel modeling approaches did tend to improve the quality of the solutions on a given grid relative to traditional models. Finally, the boundary-layer details were computed based on profiles of the wall-parallel velocity component, and it was found that a wide range of Reynolds numbers and boundary-layer thicknesses is encountered in this flow, which poses a difficult modeling task to develop suitable modeling approaches for both thin leading-edge boundary-layers that are marginally resolved with up to 5 points on even the finest grids currently achievable up to thick regions of shock-induced flow separation encountering strong adverse and spanwise pressure gradients.

### Acknowledgments

This investigation was funded by NASA (Grant Number #80NSSC20M0201) and Boeing Research & Technology. Computing resources were awarded through the Oak Ridge Leadership Computing Facility under the U.S. Department of Energy’s Advanced Scientific Computing Research Leadership Computing Challenge (ALCC) program.

### REFERENCES

- AGRAWAL, R., BOSE, S. T. & MOIN, P. 2022a Wall modeled LES of the Boeing speed bump using a non-Boussinesq modeling framework. *Annual Research Briefs*, Center for Turbulence Research, Stanford University (in preparation).
- AGRAWAL, R., WHITMORE, M. P., GRIFFIN, K. P., BOSE, S. T. & MOIN, P. 2022b Non-Boussinesq subgrid-scale model with dynamic tensorial coefficients. *Phys. Rev. Fluids* **7**, 074602.

- BOSE, S. & PARK, G. 2018 Wall-modeled large-eddy simulation for complex turbulent flows. *Annu. Rev. Fluid Mech.* **50**, 535–561.
- BRES, G. A., BOSE, S. T., EMORY, M., HAM, F. E., SCHMIDT, O. T., RIGAS, G. & COLONIUS, T. 2018 Large-eddy simulations of co-annular turbulent jet using a Voronoi-based mesh generation framework. In *2018 AIAA/CEAS Aeroacoustics Conference*, p. 3302.
- BRYSON, A. & GROSS, R. 1961 Diffraction of strong shocks by cones, cylinders, and spheres. *J. Fluid Mech.* **10**, 1–16.
- ELNAHHAS, A., AGRAWAL, R. & MOIN, P. 2022 Subgrid-scale sensitivities in wall-modeled LES of the Sandia Axisymmetric Transonic Bump. *Annual Research Briefs*, Center for Turbulence Research, Stanford University (in preparation).
- EVANS, A. N., LACY, D. S., SMITH, I. & RIVERS, M. B. 2020 Test summary of the NASA High-Lift Common Research Model half-span at QinetiQ 5-metre pressurized low-speed wind tunnel. *AIAA Paper* 2020-2770.
- FU, L., KARP, M., BOSE, S. T., MOIN, P. & URZAY, J. 2021 Shock-induced heating and transition to turbulence in a hypersonic boundary-layer. *J. Fluid Mech.* **909**, A8.
- GERMANO, M., PIOMELLI, U., MOIN, P. & CABOT, W. H. 1991 A dynamic subgrid-scale eddy viscosity model. *Phys. of Fluids A Fluid Dyn.* **3**, 1760–1765.
- GHATE, A. S., KENWAY, G. K., STICH, G.-D., BROWNE, O. M., HOUSMAN, J. A. & KIRIS, C. C. 2021 Transonic lift and drag predictions using wall-modelled large eddy simulations. In *AIAA Scitech 2021 Forum*, p. 1439.
- GOTTLIEB, S., SHU, C.-W. & TADMOR, E. 2001 Strong stability-preserving high-order time discretization methods. *SIAM Rev.* **43**, 89–112.
- GRIFFIN, K. P., FU, L. & MOIN, P. 2021 General method for determining the boundary layer thickness in nonequilibrium flows. *Phys. Rev. Fluids* **6**, 024608.
- HAM, F., MATTSSON, K. & IACCARINO, G. 2006 Accurate and stable finite volume operators for unstructured flow solvers. *Annual Research Briefs*, Center for Turbulence Research, Stanford University, pp. 243–261.
- ICHIMIYA, M., NAKASE, Y. & FUKUTOMI, J. 1993 Structure of a turbulence wedge developed from a single roughness element on a flat plate. In *Engineering Turbulence Modelling and Experiments*, pp. 613–622. Elsevier.
- LAFLIN, K. R., KLAUSMEYER, S. M., ZICKUHR, T., VASSBERG, J. C., WAHLS, R. A., MORRISON, J. H., BRODERSEN, O. P., RAKOWITZ, M. E., TINOCO, E. N. & GODDARD, J.-L. 2005 Data summary from Second AIAA computational fluid dynamics Drag Prediction Workshop. *J. Aircr.* **42**, 1165–1178.
- LEHMKUHL, O., PARK, G. & MOIN, P. 2016 LES of flow over the NASA Common Research Model with near-wall modeling. *Proceedings of the 2016 Summer Program*, Center for Turbulence Research, Stanford University, pp. 335–341.
- LEVY, D., LAFLIN, K., VASSBERG, J., TINOCO, E., MANI, M., RIDER, B., BRODERSEN, O., CRIPPA, S., RUMSEY, C., WAHLS, R., MORRISON, J., MAVRIPLIS, D. & MURAYAMA, M. 2013 Summary of data from the Fifth AIAA CFD Drag Prediction Workshop. *AIAA Paper* 2013-0046.
- LEVY, D. W., ZICKUHR, T., VASSBERG, J., AGRAWAL, S., WAHLS, R. A., PIRZADEH, S. & HEMSCH, M. J. 2003 Data summary from the First AIAA computational fluid dynamics Drag Prediction Workshop. *J. Aircr.* **40**, 875–882.
- LOZANO-DURAN, A., BOSE, S. T. & MOIN, P. 2020 Prediction of trailing edge sepa-

- ration on the NASA Juncture Flow using wall-modeled LES. In *AIAA Scitech 2020 Forum*, p. 1776.
- MARUSIC, I. & MONTY, J. P. 2019 Attached eddy model of wall turbulence. *Annu. Rev. Fluid Mech.* **51**, 49–74.
- RIVERS, M. & DITTBERNER, A. 2010 Experimental investigations of the NASA Common Research Model. In *28th AIAA Applied Aerodynamics Conference*, p. 4218.
- RIVERS, M. B., RUDNIK, R. & QUEST, J. 2015 Comparison of the NASA common research model European Transonic Wind Tunnel test data to NASA test data. In *53rd AIAA Aerospace Sciences Meeting*, p. 1093.
- RUMSEY, C. L. & SLOTNICK, J. P. 2015 Overview and summary of the Second AIAA High-Lift Prediction Workshop. *J. Aircr.* **52**, 1006–1025.
- RUMSEY, C. L., SLOTNICK, J., LONG, M., STUEVER, R. & WAYMAN, T. 2011 Summary of the first AIAA CFD high-lift prediction workshop. *Journal of Aircr.* **48**, 2068–2079.
- RUMSEY, C. L., SLOTNICK, J. P. & SCLAFANI, A. J. 2019 Overview and summary of the Third AIAA High-Lift Prediction Workshop. *J. Aircr.* **56**, 621–644.
- RUMSEY, C. L., SLOTNICK, J. P. & WOEBER, C. 2022 HLPW-4/GMGW-3: Overview and workshop summary. In *AIAA AVIATION 2022 Forum*, p. 3295.
- TINOCO, E. N. 2020 Analysis of the transonic NASA Common Research Model at high angle of attack. In *AIAA Aviation 2020 Forum*, p. 2745.
- TINOCO, E. N., BRODERSEN, O. P., KEYE, S., LAFLIN, K. R., FELTROP, E., VASSBERG, J. C., MANI, M., RIDER, B., WAHLS, R. A., MORRISON, J. H. *et al.* 2018 Summary data from the Sixth AIAA CFD Drag Prediction Workshop: CRM cases. *J. Aircr.* **55**, 1352–1379.
- VASSBERG, J. C., TINOCO, E. N., MANI, M., BRODERSEN, O. P., EISFELD, B., WAHLS, R. A., MORRISON, J. H., ZICKUHR, T., LAFLIN, K. R. & MAVRIPLIS, D. J. 2008 Abridged summary of the Third AIAA computational fluid dynamics Drag Prediction Workshop. *J. Aircr.* **45**, 781–798.
- VASSBERG, J., TINOCO, E., MANI, M., RIDER, B., ZICKUHR, T., LEVY, D., BRODERSEN, O., EISFELD, B., CRIPPA, S., WAHLS, R. *et al.* 2010 Summary of the Fourth AIAA CFD Drag Prediction Workshop. In *28th AIAA Applied Aerodynamics Conference*, p. 4547.
- VREMAN, A. 2004 An eddy-viscosity subgrid-scale model for turbulent shear flow: Algebraic theory and applications. *Phys. Fluids* **16**, 3670–3681.
- WHITMORE, M. P., GRIFFIN, K. P., BOSE, S. T. & MOIN, P. 2021 Large-eddy simulation of a Gaussian bump with slip-wall boundary conditions. *Annual Research Briefs*, Center for Turbulence Research, Stanford University, pp. 45–58.